6 Synthesis and characterization of La^{3+} doped system $SrCe_{1-x}La_xO_3$ (x=0.0,0.02,0.04,0.06 and 0.10)

6.1 Introduction

Proton conducting electrolyte materials are of big interest which is because of their many applications especially fuel cell, gas sensors, hydrogen separation membrane or high temperature electrolyze [237-239]. Application of proton conducting perovskite type oxides appear to be an attractive alternative as solid electrolytes for Solid Oxide Fuel Cells (SOFC) to that of well-known oxygen ions conducting electrolytes. Opposite direction of H^+ flow in the electrolyte (in the relation to movement of O^{2-}) alters the nature of electrochemical reactions take place at concerned electrodes which is very useful from the practical point of view. Since water is produced at air electrode (cathode) side, hydrogen fuel is not diluted, permitting for its complete utilization [129]. In addition to that, for such cell working in electrolysis mode, pure hydrogen could be produced (and compressed), without any additional gas separation or purification processes. Ultimately, usage of proton conducting electrolyte permit to maintain high value Nernst voltage in the cell and it relegates instability problem at anode since no water vapor is present there [129].

Since, pioneer works about proton conductivity (Sr, Ba)(Ce, Zr)$O_{3-\delta}$ oxides by Iwahara et al. [129], many proton conducting perovskite oxides have been investigated, indicating wide range of properties, concerning facilitation of incorporation of water into the structure and different value of proton conductivity at high temperatures [242, 243]. Out of them, acceptor type doped cerium based oxides have high proton conductivity containing water vapor atmospheres with high H^+ transference number at elevated temperatures [244]. Ce site doping with selected lanthanides is important to induce the presence of oxygen nonstoichiometric which play crucial role for proton conductivity to take place. Present oxygen vacancies are absolutely necessary for water incorporation into the lattice during which process $OH_O^{\bullet}$ are being formed reversibly in such materials [247]. Many investigations have been explored

regarding modification of present material strontium cerate $SrCeO_3$ by doping with Y, Tm, Sm, Sc, Mg, Ho, Eu, Nd, Yb and Tb [237, 238, 74, 239]. Good proton conductivity has been noticed generally for example terbium doped $SrCe_{0.95}Tb_{0.05}O_{3-\delta}$ showing high value of conductivity 10^{-3}-10^{-2} Scm^{-1} in the range of 500 – 900 ºC in methane or hydrogen containing atmosphere [264]. If we consider crystal structure, most of the papers report unmodified orthorhombic symmetry with Pnma space group which is also inspected for undoped $SrCeO_3$ material [194]. Properties of La-doped on alkaline earth site of perovskite oxides, $MSnO_3$ (M= Ba, Sr and Ca) have been investigated widely for transparent conducting oxide, humidity sensor, electrode material for IT-SOFC [265]. La-doped $SrSnO_3$ and $BaSnO_3$ have been used for various applications such as humidity sensor, transparent conducting oxides, proton conducting electrolyte in fuel cells, etc. [266, 267]. The interesting properties of La-doped perovskite stannates motivated us to synthesize and study the effect of La doping on the electrical property of perovskite $SrCeO_3$ to explore its applications.

6.2 Experimental

The system $SrCe_{1-x}La_xO_{3-\delta}$ with x = 0.00, 0.02, 0.04, 0.06 and 0.10, abbreviated respectively as SCL0, SCL2, SCL4, SCL6 and SCL10 have been prepared by auto combustion synthesis. $Sr(NO_3)_2$ (Purity 99.9%, Alfa Aesar), cerium ammonium nitrate $(NH_4)_2Ce(NO_3)_6$ (Purity 99.5%, Alfa Aesar) and lanthanum nitrate hydrate $La(NO_3)_3.H_2O$ have been used as raw materials as well as sucrose as a fuel to synthesize the system $SrCe_{1-x}La_xO_{3-\delta}$. Details of the experimental procedures were already reported in chapter 2.

Details of the experimental procedures were already reported in chapter 2. Silver (Ag) and platinum (Pt) paste were used as electrode on both faces of the sintered pellets and fired for 20 minutes at 700 °C. In order to understand the mixing of dopants in $SrCeO_3$, the crystal structure of the doped $SrCeO_3$ sample was analyzed using X-ray Diffractometer (XRD). The surface morphology was studied by using scanning electron microscopy (SEM) equipped with

an X-ray energy dispersive spectrometer (EDS). The electrical conductivity of prepared sintered pellet was measured by employing two-probe impedance spectroscopy LCR meter (Agilent - 4980 A, USA) in the temperature range 100°C-600 °C.

6.3 Results and Discussions

6.3.1 Thermal analysis (TGA/DSC)

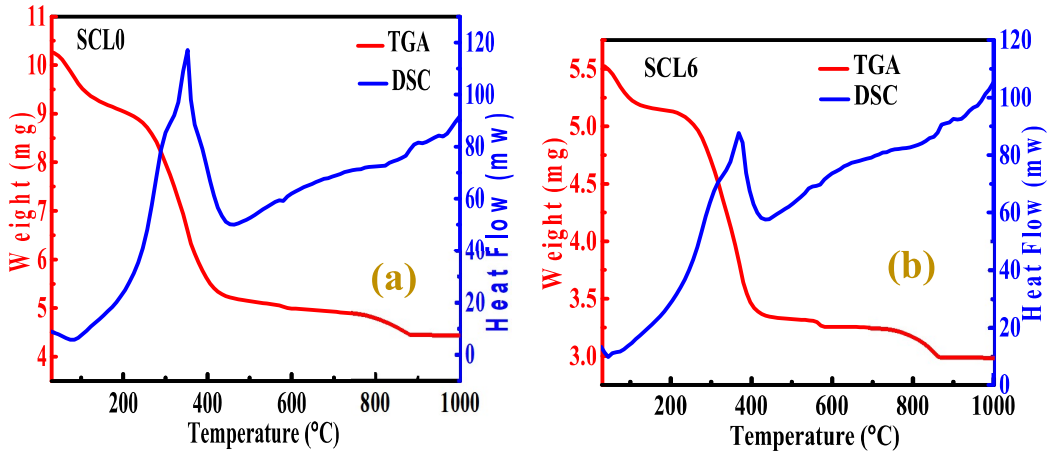

Figure 6.1 Thermo gravimetric analysis (TGA) and differential scanning calorimetric (DSC) curves.

Figures 6.1 (a)-(b) show thermogravimetric (TG) and differential scanning calorimetry (DSC) curves for two representative samples SCL0 and SCL6, respectively. Similar curves were recorded for other samples also. From the TGA curves, it is observed that the samples have small weight loss at around 100 °C and a large weight loss in the temperature range $200^0C - 400^0C$. The DSC curves have an endothermic local minimum at 100 °C and an exothermic local maximum around 370 °C which is considered as burning of residual organic compounds. The weight loss around 100 °C may be due to the evaporation of moisture from the sample which is an endothermic reaction. Between 200 °C and 400°C, most of the unburned carbon in the samples undergo combustion, an exothermic reaction, and escape along with other volatile compounds. There is another small weight loss in the temperature range 700 – 800°C which

may be assigned to the decomposition of $SrCO_3$ into SrO. No weight loss in the samples above 900 °C confirmed that the formation of the compounds is complete by 900 °C. Hence, the calcination temperature was fixed at 1000 °C.

6.3.2 Phase identification using XRD

Room temperature powder X-ray diffraction pattern of all the samples has been recorded and shown in **Figure 6.2**. The absence of any extra peaks corresponding to starting materials or secondary phase confirmed the formation of single phase solid solution for all the compositions. All the doped samples crystallized in orthorhombic structure with space group Pnma. The peaks present in the diffraction pattern of samples are intense, indicating good crystallinity of the synthesized powders.

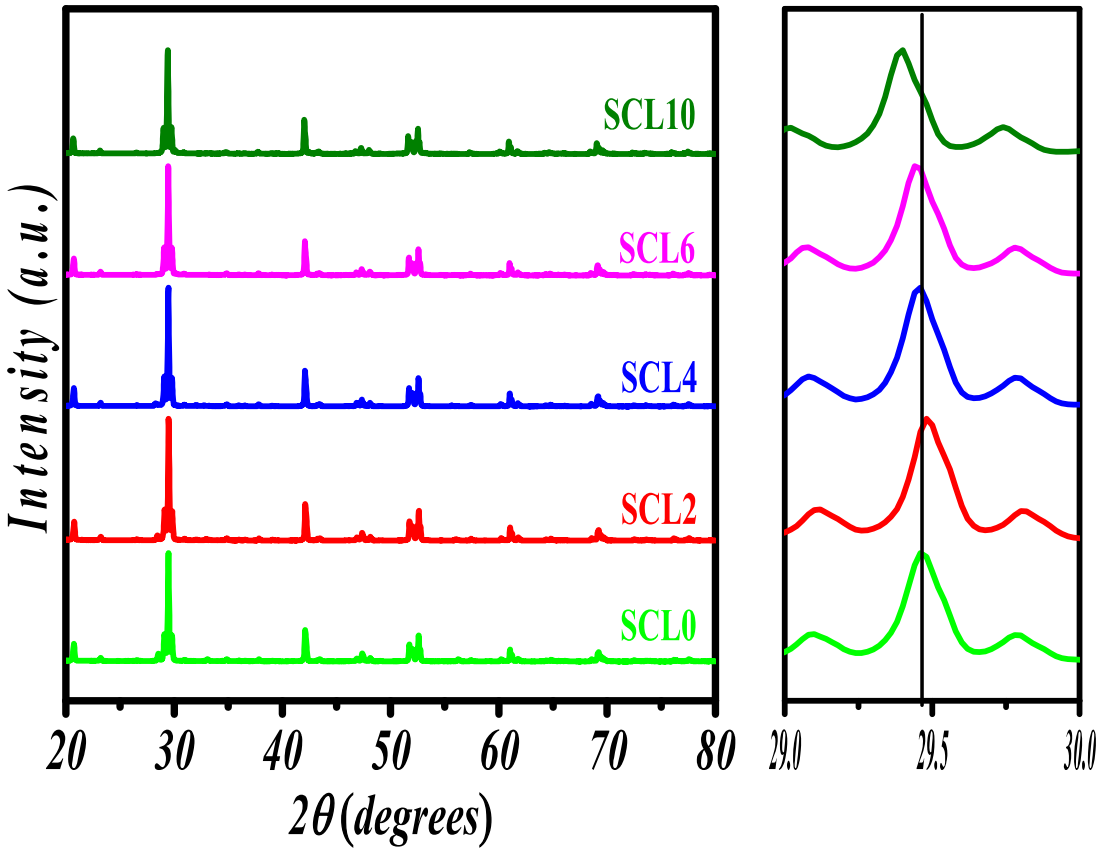

Figure 6.2 Room temperature powder X-ray diffraction pattern of all samples.

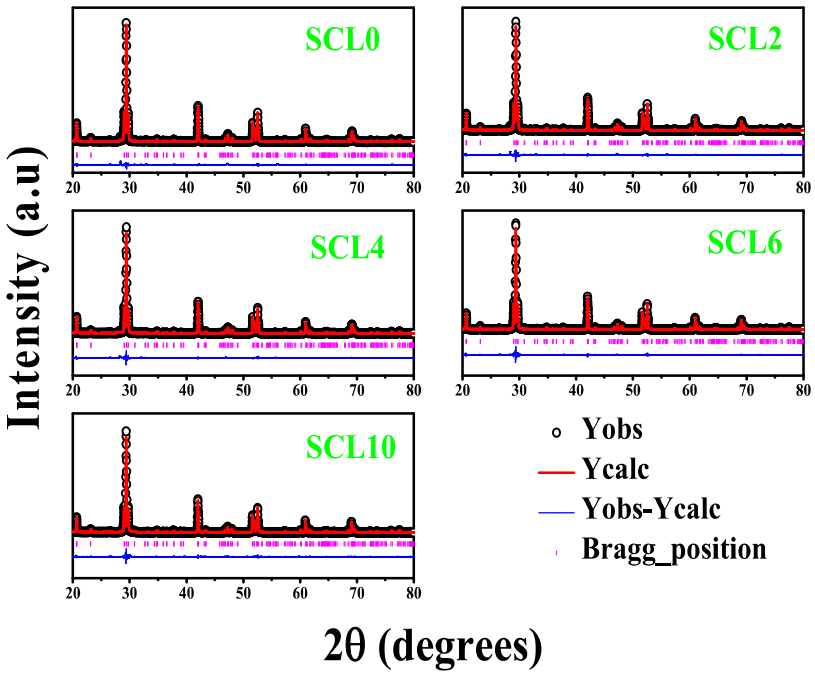

Figure 6.3 Rietveld refinement of X-ray diffraction the system SrCe1-xLaxO3.

It has also been observed that the diffraction peaks slightly shift towards higher angle with the 'La' substitution up to x = 0.02. With the further increase in 'La' substitution, the peak shifts towards lower angle for higher concentration upto x = 0.10. To illustrate this, highest peak intensity corresponding to $2\theta \approx 29.5^{o}$ is shown in **Figure 6.2** right side. The shift of diffraction peaks towards lower angle with increasing concentration of 'La' can be attributed to the larger size of substituent ions like the ionic radius of La^{3+} (1.03 Å) is larger than that of Ce^{4+} (0.87 Å).

To get detailed structural parameters of the synthesized samples the Rietveld refinement of the X-ray diffraction patterns are carried out using 'FullProf software suite'. Pattern observed experimentally, calculated theoretically and their differences for all the samples are shown in **Figure 6.3**. The refinement process has already been described in Chapter 3. The structural parameters such as lattice parameter, unit cell volume, and other relevant parameters

along with reliability factors R_p, R_{wp}, $R_{f,}$ and χ^2 are given in Table 6.1. The value of goodness of fit ($S = R_{wp}/R_p$) parameter is lying in between 1.02 – 1.22 reasonable for assigning the structure strontium cerate for doped samples.

Table 6.1 Various parameters obtained from Rietveld refinement analysis of XRD data of the prepared system $SrCe_{1-x}La_xO_3$ ($0.00 \leq x \leq 0.10$).

Samples Code	Lattice Parameters (Å)				χ^2	Density (g/cm^3)
	a	b	c	Cell Volume $(Å)^3$		
SCL0	6.1507	8.5848	6.0091	317.30	1.24	5.79
SCL2	6.1198	8.5840	6.0082	317.17	1.45	5.81
SCL4	6.1509	8.5858	6.0083	317.29	1.74	5.77
SCL6	6.1536	8.5890	6.0089	317.59	1.49	5.75
SCL10	6.1572	8.5941	6.0099	318.02	1.32	5.74

The crystallite size has been determined using Size-Strain Plot (SSP) method. Detailed procedure of determining crystallite size has been described in Chapter 2 using **Eq. (2.21)**. According to the **Eq. (2.21)**, plots of $\left(\frac{d_{hkl}\beta cos\theta}{\lambda}\right)^2$ vs. $\left(\frac{{d_{hkl}}^2\beta cos\theta}{\lambda^2}\right)$ for all samples are shown in **Figure 6.4**. In this plot, value of the crystallite size is determined from the slope of the linear fitting of the data. The square root of the intercept on y-axis gives the value of lattice strain.

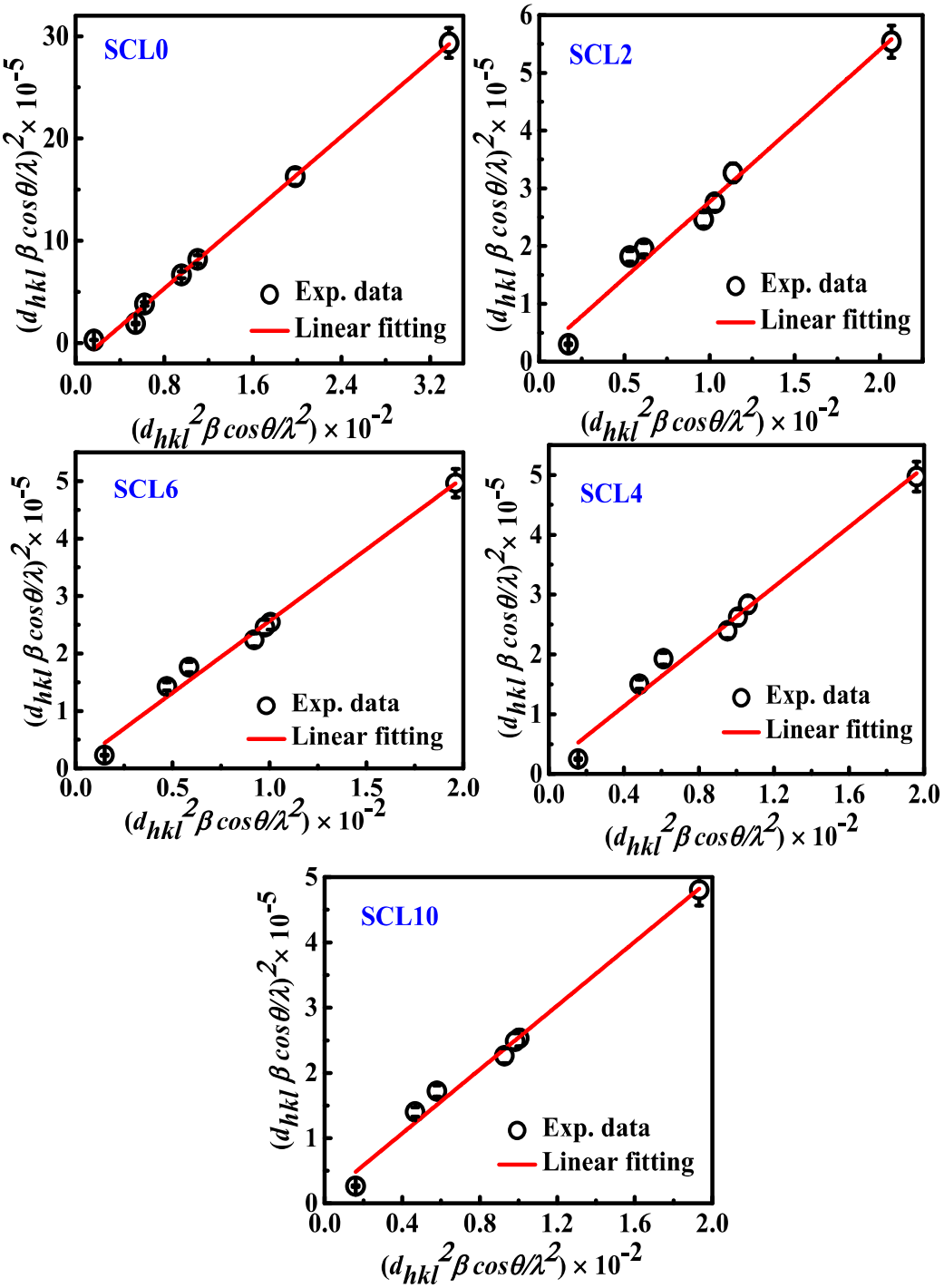

Figure 6.4 Size Strain plots (SSP) for determination of crystalline size and lattice strain of the samples.

The obtained values of crystallite size and lattice strain for all the samples are given in Table 6.2. Further, it is observed that the value of lattice strain for all the La-doped samples is less than undoped sample. The lower value of lattice strain observed for doped samples is may be due to larger ionic radii of the La^{3+} than Ce^{4+} ion.

Table 6.2 Various parameters for the powders obtained by calcination at 1100 ºC for 12 h.

Samples Code	Crystallite size (nm)	Lattice strain (ε)x10^{-3}	Grain Size ((μm)	Optical band Gap (eV)	Electrical Conductivity (S.cm^{-1}) at 600 °C	Activation Energy (eV) 300 – 600 ºC
SCL0	49.94	9.20	2.32	3.12	3.99 x10^{-5}	1.09
SCL2	55.70	2.29	5.86	3.26	6.84 x10^{-4}	1.04
SCL4	57.92	2.32	5.20	3.36	1.12 x10^{-3}	0.99
SCL6	58.30	1.66	5.77	3.28	2.29 x10^{-5}	0.93
SCL10	59.11	1.93	3.55	3.31	2.82 x10^{-6}	0.89

6.3.3 Raman Spectrum Analysis

The Raman spectroscopy is a simple and non-destructive tool to probe structural information at single unit cell level. In this work, Raman technique has been used to study the incorporation of La^{3+} ions at Ce-site of $SrCeO_3$ and to detect the impurity phase present in trace amount. It has been reported that the arrival of impurity phases namely CeO_2, $SrCO_3$ and Sr_2CeO_4 is inevitable in the powder of strontium cerate ($SrCeO_3$) synthesized by any technique. The similarity in the XRD pattern of $SrCeO_3$ and Sr_2CeO_4, it is difficult to detect the impurity phase Sr_2CeO_4 by using XRD technique only. It has been found from the literature survey that Raman spectra of $SrCeO_3$ and Sr_2CeO_4 is different completely. Besides, Raman measurement can explore lower concentration of impurity phase and more sensitive than that of XRD as well. Hence, the room temperature Raman spectra has been recorded in wave number range 100 – 800 cm^{-1} (shown in **Figure 6.5**) to check the purity of synthesized samples.

From the spectra, it is found that the most intense Raman band appear at 340 cm^{-1} in the spectra of all prepared samples. In addition to that, this intense band has two satellite band at 370 cm^{-1} and 314 cm^{-1} are also observed in the spectra of all prepared samples. The spectra and positions of various bands synthesized in this work for $SrCeO_3$ (SCL0) are in deal with Raman spectra recorded by earlier workers [268]. This outcome ensures a high purity powder formation of SrCeO3. The Raman spectra of La - doped samples (SCL2, SCL4, SCL6, and SCL10) are similar to that of undoped samples $SrCeO_3$ (S1Gd0). This shows that crystal structure of La - doped samples remains unaltered even by increasing concentration of La up to 10 mol %. Kosacki et. al [234] given that 105, 116, 140, 180 cm^{-1} bands are due to motion of Sr cations because intensity and frequency of these bands independent of dopant ion concentration. The Raman bands at 312, 340 and 370 cm^{-1} may be connected with vibration involving oxygen ions. The highest intensity bands noticed at 340 cm^{-1} in Raman spectra of all prepared samples is ascribed to Ce – O stretching vibration mode associated with CeO_6

octahedral. The frequency and shape is changed with La^{3+} concentrations. As Ce^{4+} ions occupy a centrosymmetric site in the structure of $SrCeO_3$. The Raman active Ce - O vibrations involving oxygen ions motion [226]. On substitutions of La^{3+}, there is small shift (2 cm^{-1}) in the position of this band toward higher wavelength side has been observed for all compositions. The change in the position and shape of the bands for doped samples confirms the substitution of La at Ce site of $SrCeO_3$ (see right top of **Figure 6.5**).

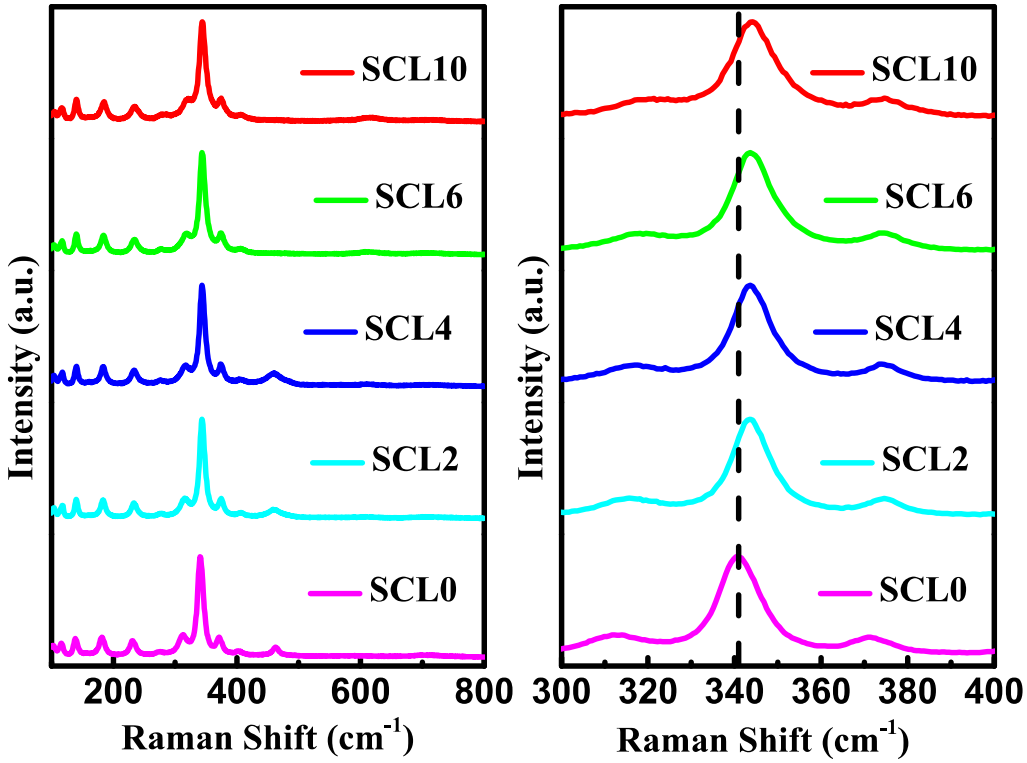

Figure 6.5 Room temperature Raman spectrum of the prepared samples.

6.3.4 Fourier Transform Infrared Spectroscopy (FTIR) analysis

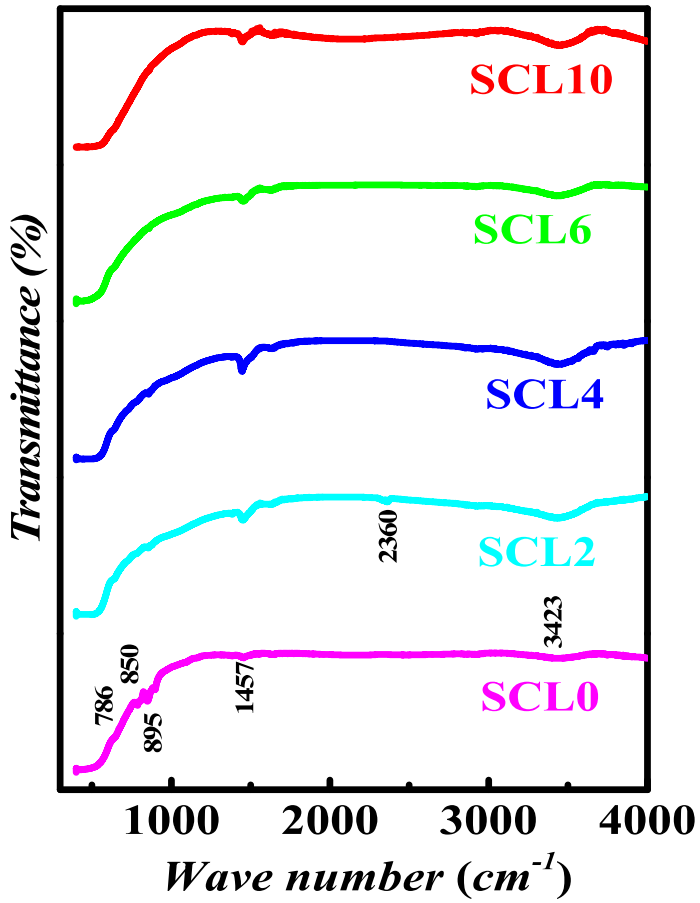

Figure 6.6 Fourier transformed infra-red (FTIR) spectra of all prepared samples.

Fourier Transform Infrared (FTIR) technique is the sensitive technique for detection of impurities phase based on alkaline earth carbonates and phase formation as well. This technique can have searched out concentrations of ≤ 6% of alkaline earth carbonates. Hence, to find out the existence of strontium carbonate ($SrCO_3$) in the synthesized samples, FTIR spectra of the samples (shown in **Figure 6.6**) has been carried out. The FTIR spectra of undoped samples $SrCeO_3$ (SCL0) is in consent with earlier reports [228]. The FTIR spectra of La^{3+} doped samples are similar to the undoped samples as well. An incomplete broadband below 500 cm^{-1} is noticed which is ascribed to the Ce – O vibration in CeO_6 octahedral in the spectra

of all samples. Two bands noticed at 850 and 1457 cm^{-1} are probably attributed to C – O vibrations due to unavoidable amount of $SrCO_3$ in the spectra of all prepared samples.

6.3.5 UV-Visible Spectroscopy

The Ultraviolet-visible (UV) spectroscopy technique has been used to investigate the optical absorbance of the undoped $SrCeO_3$ and La-doped $SrCeO_3$. The room temperature UV spectrum of the samples recorded in the wavelength range 200-800 nm is shown in **Figure 6.7**. There is a strong absorption band below 400 nm in the spectra of all prepared samples. On substitution of La^{3+}, the position of the absorption maxima unaltered on further increase in the concentration. The energy difference between highest occupied molecular orbital (HOMO) and lowest unoccupied molecular orbital (LUMO) is designated as optical band gap (E_g) [257]. The Tauc's plot for direct band transition have been created from UV- visible absorption data using **Eq. (2.23)** as discussed in chapter 2. The direct band gap of any material is termed as the transition between the lower edges of HOMO to the upper edge of the LUMO. The direct band has been obtained from the intercept of linear region for $(\alpha h\vartheta)^2 = 0$ at energy axis. The optical band gap of prepared samples has been extracted from the Tauc's plot is presented in Table 6.2. From Table 6.2, it is noticed that the value of direct band gap of La^{3+} doped samples is higher than that of undoped sample.

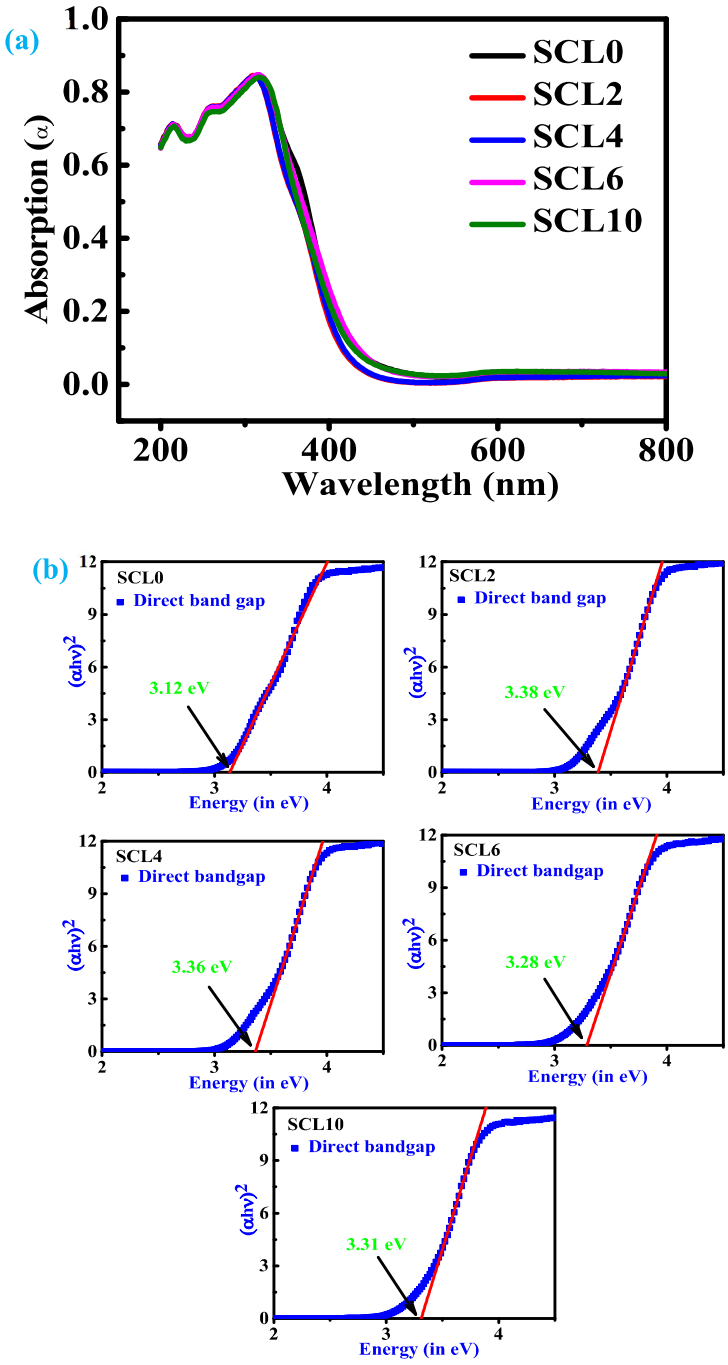

Figure 6.7 (a) UV- visible absorption spectra and **(b)** Tau plots received from the absorption data *of* the prepared system $SrCe_{1-x}La_xO_3$ ($0.00 \leq x \leq 0.10$).

6.3.6 Microstructural study using SEM

The surface morphology of the samples has been studied using scanning electron microscopy (SEM). **Figure 6.8** displays the SEM images of the fracture surface of sintered pellets of all compositions of the prepared samples. A look on SEM image indicates that all the prepared samples are having the fine grains of irregular shape and size. It also shows that all the samples have some porosity. In addition, the compositional homogeneity has been probed by recording energy dispersive X-ray (EDX) spectrum of different region of the fractured surface of the pellets. EDX spectrum of one of the random chosen region indicate the presence of the peaks corresponding to Sr, Ce, La and O elements only.

In order to determine the average grain size of the prepared samples, the histograms distribution (shown in **Figure 6.9**) of prepared samples have been obtained by using **Image J** software. By the Gaussian function fitting to these histograms, the average grain size of prepared samples has been derived and listed in Table 6.2. It is observed from Table 6.2 that average grain size of the prepared samples higher than that of undoped sample.

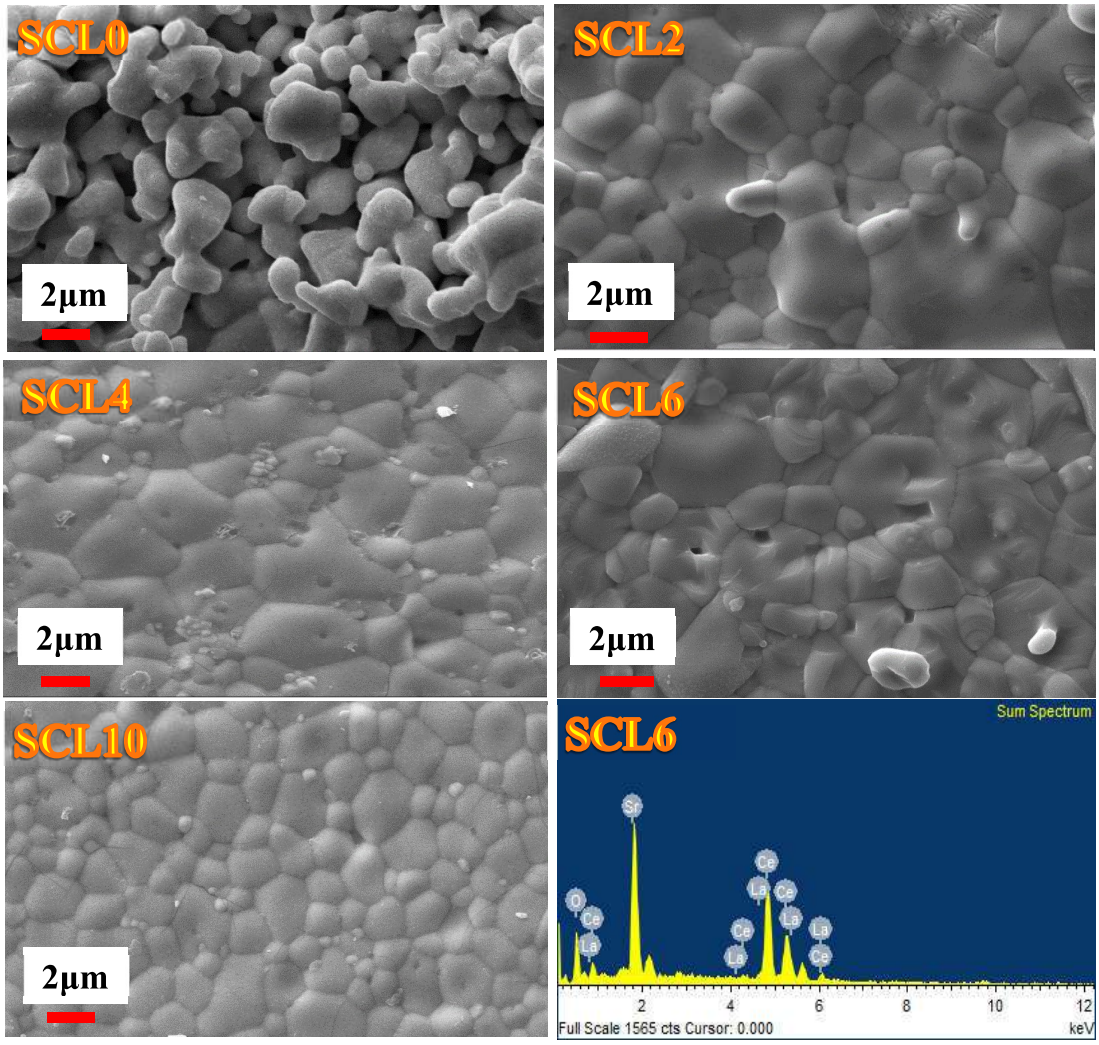

Figure 6.8 Scanning electron micrograph (SEM) of fractured surfaces of the prepared samples & EDXA spectrum of SCL6.

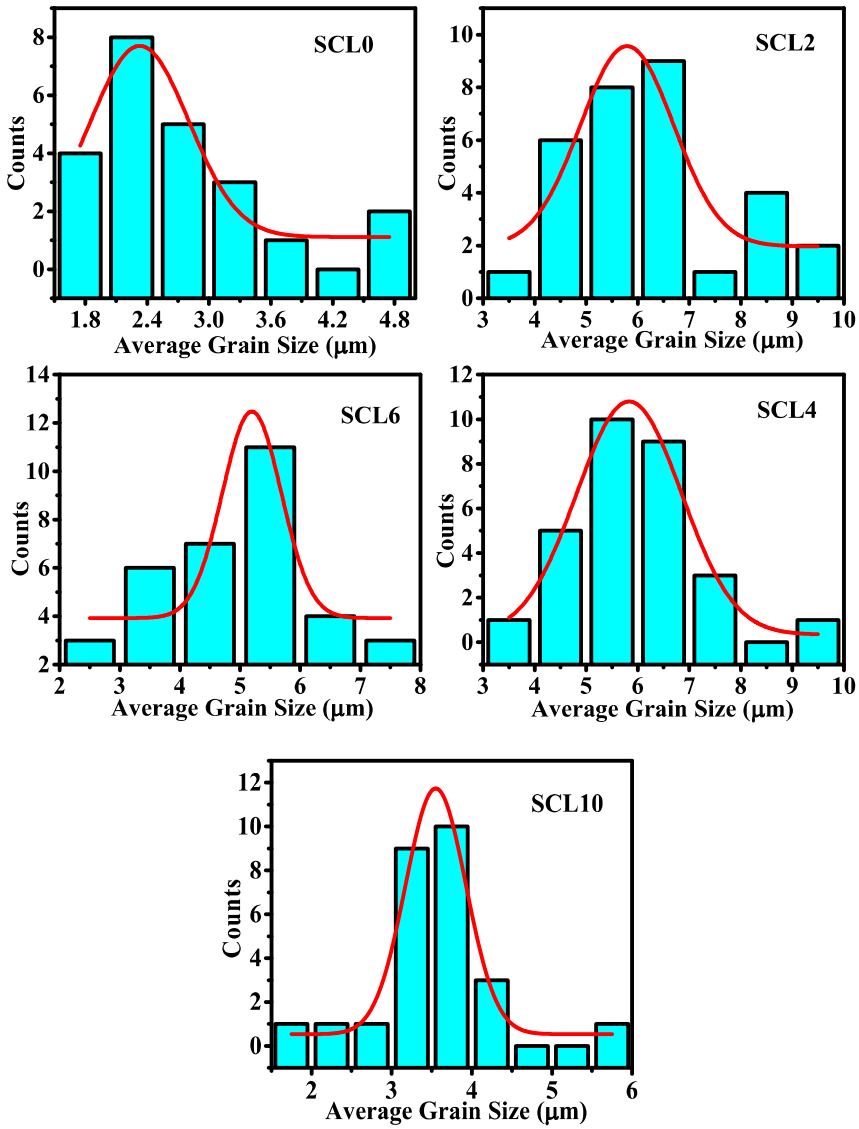

Figure 6.9 Histograms grain size distribution of the samples.

6.3.7 Transmission Electron Microscope (TEM) Analysis

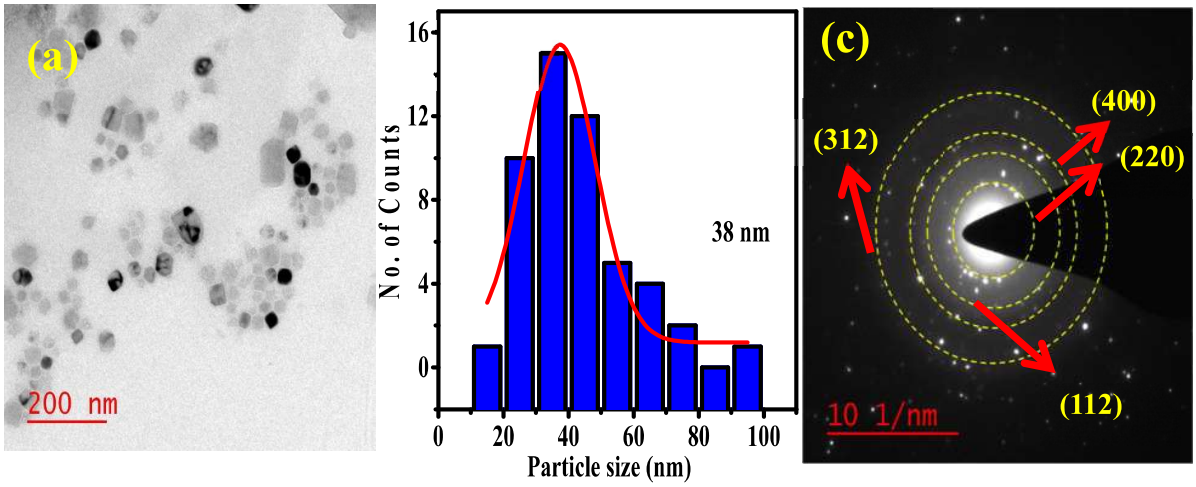

Figure 6.10 (a) Transmission electron micrograph of a representative sample SCL10, **(b)** Distribution function fitted with Gaussian Function and **(c)** Selected Area Electron Diffraction (SAED) pattern.

The particle size of the synthesized samples has been determined by transmission electron microscopy (TEM). The bright field image of a representative sample SCL10 is shown in **Figure 6.10**. The morphology reflects spherical shape of particles. The particle size is determined using "**Image J**" software (see **Figure 6.10 (b)**). The average particle size is determined by fitting Gaussian function to the histogram of distribution of particle size. The average particle size of the sample is found to be 38 nm. The selected area electron diffraction (SAED) pattern as shown in **Figure 6.10 (c)** consists of regular ring pattern with bright spot typical nature of polycrystalline sample. These rings pattern corresponds to Miller planes (hkl) of unit cell of $SrCeO_3$. The planes with their Miller indices as indexed in **Figure 6.10 (c)** are in agreement with XRD result.

6.3.8 Impedance spectroscopy

This is an emphatic and simple tools to investigate the electrical properties of polycrystalline materials. It makes possible for polycrystalline materials to separate out the contribution of different parts i.e. grains, grain boundary and electrode specimen interface from the total impedance for the electrical conductivity [250]. Hence, this tool is applied to analyse the influence of La^{3+} doping on the electrical properties of the prepared samples. In order to study the evolution of impedance with temperatures, the complex plane impedance plots have been drawn at different temperature of all prepared samples. Out of these plots, a few plots as a representative for sample SCL2 with nonlinear curve fitting are depicted in **Figure 6.11 (a) - (f)**. From the figure, it can be noticed that a part of one depressed semi-circular arc appears at 300 ºC which grows with rise of temperature having tendency to complete this arc. With ahead rise in temperature, a part of depressed semi-circular arc is appeared with a tail at one end again. This is because of decrease in relaxation time of different contributions with increase in temperature. The capacitance corresponding to semi-circular arc has been calculated by using relation $\omega\tau = 2\pi fRC = 1$.

Where $R, C, f and\ \tau$ are peak resistance, capacitance, frequency and relaxation time respectively that holds good at the peak of corresponding semi-circular arc. The value of capacitance is found to be of the order of 10^{-11} F. It is reported that the capacitance of grains of polycrystalline ceramic oxides fall in the range pF ($10^{-12} – 10^{-10}$ F) while of the grain boundaries lie in the range of nF ($10^{-9} – 10^{-8}$ F). Hence the attained value of capacitance demonstrates that the observed high frequency semi-circular arc can be ascribed to the electrical conduction through the bulk.

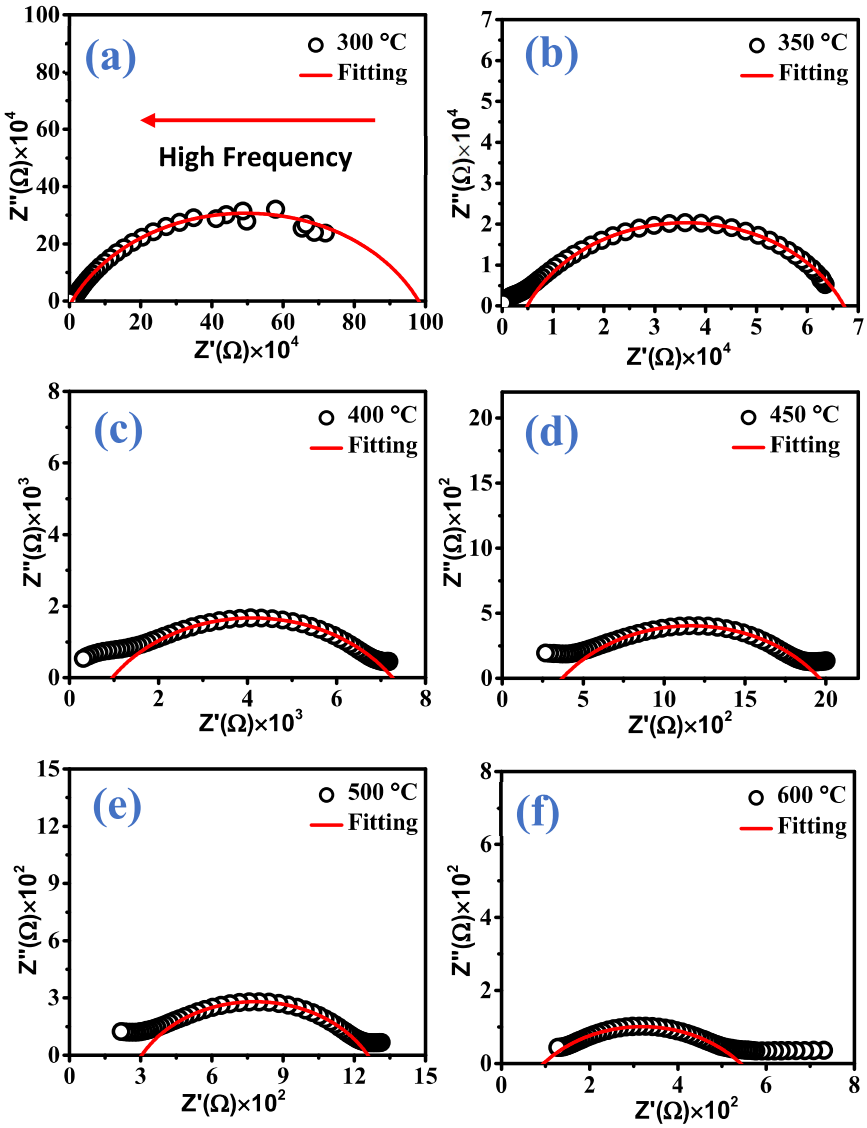

Figure 6.11 Complex plane Impedance plots for the sample SCL2 at **(a)** 300 ˚C **(b)** 350 ˚C **(c)** 400 ˚C **(d)** 450 ˚C **(e)** 500 ˚C and **(f)** 600 ˚C

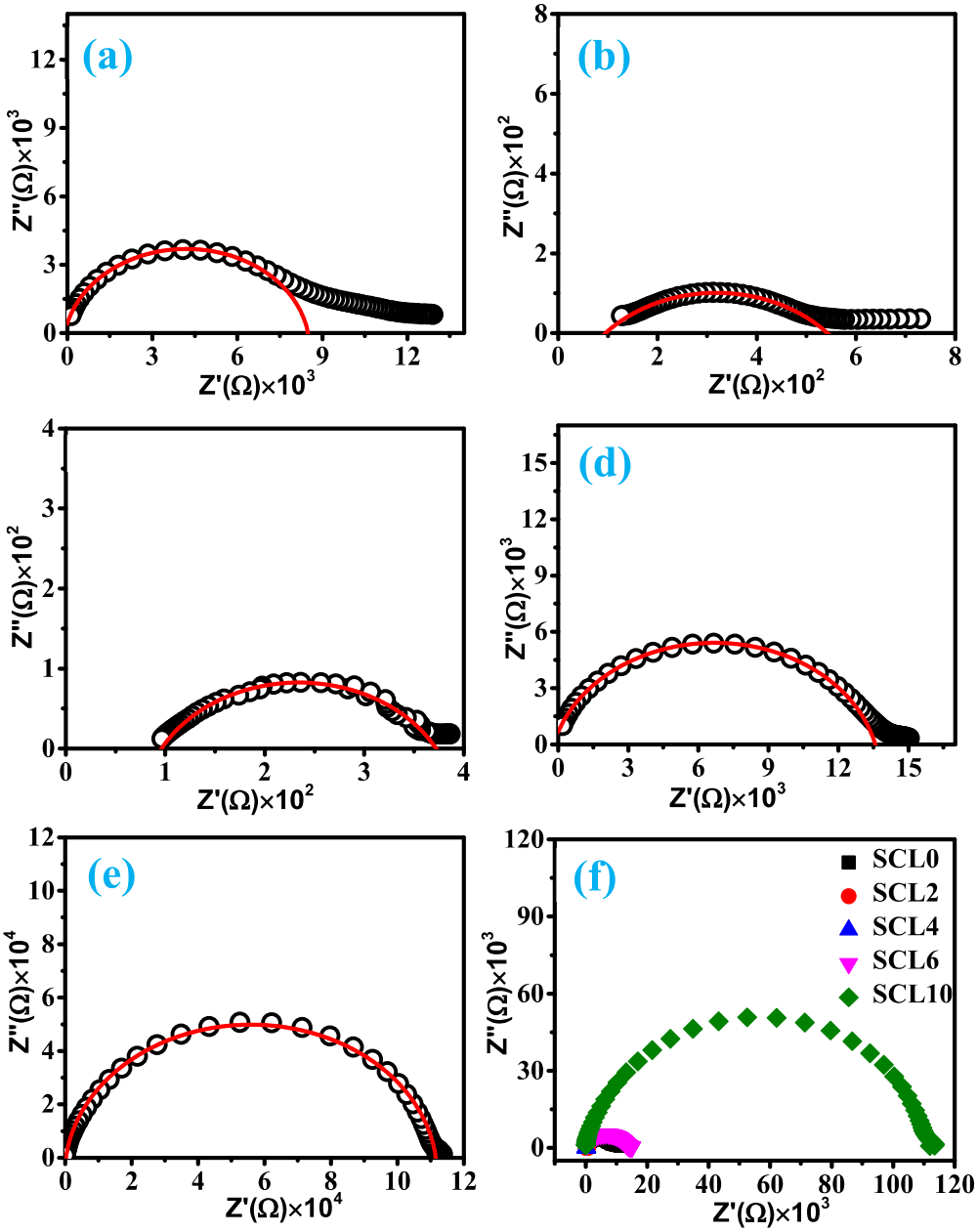

Figure 6.12 The complex plane impedance plots for compositions: **(a)** SCL0 **(b)** SCL2, **(c)** SCL4 and **(d)** SCL6 and **(e)** SCL10 **(f)** combined plot for $SrCe_{1-x}La_xO_3$ ($0.00 \leq x \leq 0.10$): at 600 °C.

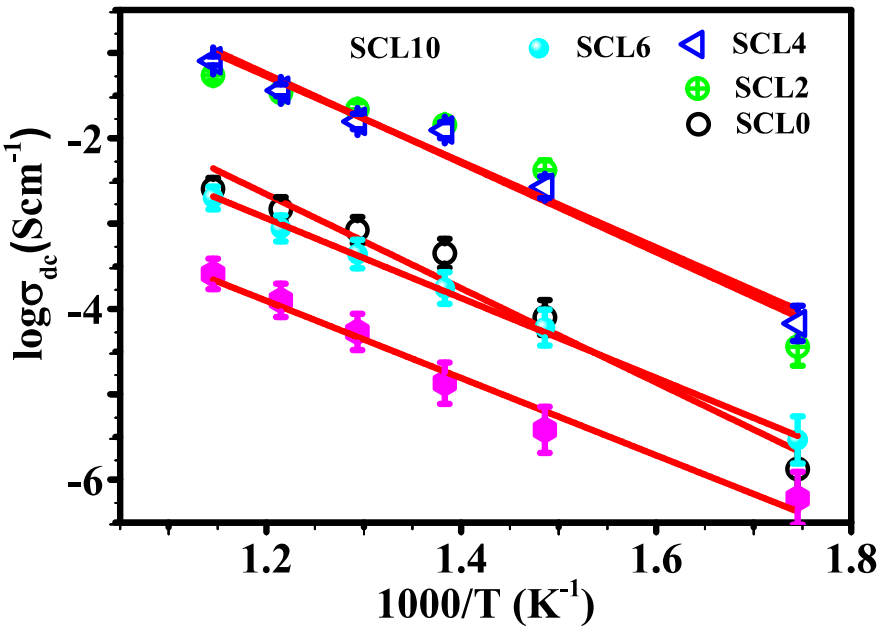

Figure 6.13 DC conductivity of all composition SCL0, SCL2, SCL4, SCL6 and SCL10 for system $SrCe_{1-x}La_xO_3$ ($0.00 \leq x \leq 0.10$).

In order to show the variation of impedance of all composition of prepared system, the complex plane impedance plots with nonlinear curve fitting are depicted in **Figure 6.12 (a) - (f)**. Where **Figure 6.12 (a) - (e)** show the separate plots for each composition of prepared system at 600 ºC and **Figure 6.12 (f)** represents the combined plots. **Figure 6.12** clearly indicates that the sample SCL4 has the lowest impedance.

Here, total resistance of the samples can be obtained from the intercept of the depressed semi-circular arc on the real axis while the conductivity of samples can be calculated by using **Eq. (5.3).** The total conductivity of all composition of samples have been calculated and tabulated in Table 6.2 and it is observed from the table that conductivity found to be order of 10^{-3} Scm^{-1} for sample SCL4 which is maximum among all prepared composition at 450 °C.

Figure 6.13 shows the Arrhenius plots of $log\ \sigma$ versus $1000/T$ for all composition of the prepared system $SrCe_{1-x}La_xO_3$. The activation energy of the conduction for all composition has been calculated from the slope of the plots $log\ \sigma$ versus $1000/T$ applying the Arrhenius relationship **Eq. (5.4)**. **Figure 6.13** clearly indicates that the sample SCL4 possess higher conductivity than other samples. The activation energy calculated for all composition of the samples is presented in Table 6.2.

The change in electrical conductivity with La^{3+} doping on Ce^{4+} may be explained by defect chemistry

$$La_2O_3 \xrightarrow{SrCeO_3} 2La_{Ce}{}' + V_{\ddot{O}} + 3O_0{}^x + \frac{1}{2}O_2(g) \qquad (6.1)$$

6.3.9 X-ray Photoelectron Spectroscopy (XPS) analysis

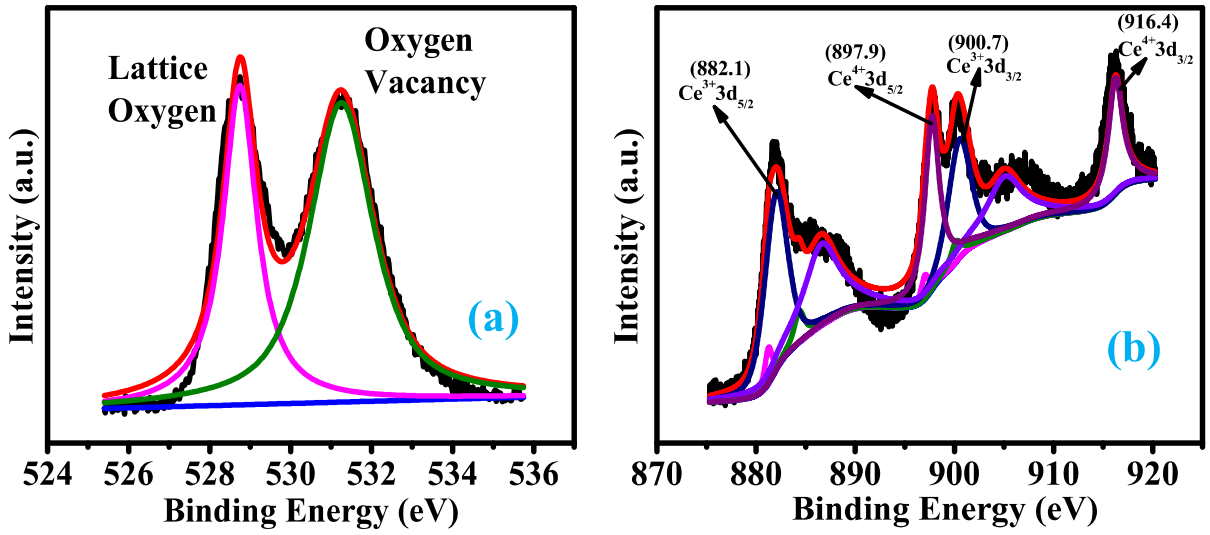

Figure 6.14 (a) Deconvoluted XPS of O 1s profile **(b)** Deconvoluted XPS of Ce 3d profile of sample $SrCe_{0.96}La_{0.04}O_3$ (SCL4).

The X - ray photoelectron spectroscopic technique is used to reveal the valence state of the constituent element present in the composition and existence of oxygen vacancy. In this work, we reported the XPS spectrum of one sample SCL4. The valance states of various elements are determined from the High resolution XPS spectrum (HRXPS) for each element. **Figure 6.14 (a)** displays XPS spectrum of O 1*s*; two peaks at 528.90 eV and 531.28 eV. The lower binding energy (528.90 eV) peak is associated with lattice oxygen, whereas the higher binding energy (531.45 eV) normally corresponds to oxygen vacancies [250]. **Figure 6.14 (b)** depicts the HRXPS spectrum for Ce. The peaks noticed at particular binding energies were matched with binding energy value for Ce^{3+} and Ce^{4+} reported in the literature [235]. Presence of four peaks of Ce^{4+} $3d_{3/2}$ (916.4), Ce^{4+} $3d_{5/2}$ (897.9), Ce^{3+} $3d_{3/2}$ (900.7) and Ce^{3+} $3d_{5/2}$ (882.1) for sample SCL4 has clearly indicated existence of Ce in both Ce^{3+} and Ce^{4+} states.

6.4 Conclusions

A few compositions of solid solution $SrCe_{1-x}La_xO_3$ (x=0.0, 0.02, 0.4, 0.6 and 0.10) have been synthesized by auto combustion technique, calcined at 1100 °C. Retvield refinement of XRD data has confirmed orthorhombic crystal structure and Pnma space group for all the samples. The crystal structure, lattice strain and crystallite size have been calculated. The incorporation of La has been studied by Raman and Fourier's transformation of infrared (FTIR) spectroscopy, which reconfirm that synthesized powders are single phase. The optical band gaps of the samples have determined from absorption data using Tauc plot. SEM images of sintered samples exhibited increase in the average grain size on increasing lanthanum concentration. Results of complex plane impedance analysis revealed that composition with x=0.04 has highest value of conductivity ($1.12x10^{-3}$ Scm^{-1}). XPS studies has indicated presence of Ce in mixed valence state (both Ce^{3+} and Ce^{4+} states).